



HAL
open science

Optimal multiple motion encoding in Phase-Contrast MRI

Helge Herthum, Hugo Carrillo, Axel Osses, Sergio Uribe, Ingolf Sack,
Cristobal Bertoglio

► **To cite this version:**

Helge Herthum, Hugo Carrillo, Axel Osses, Sergio Uribe, Ingolf Sack, et al.. Optimal multiple motion encoding in Phase-Contrast MRI. 2020. hal-02947225v1

HAL Id: hal-02947225

<https://hal.science/hal-02947225v1>

Preprint submitted on 23 Sep 2020 (v1), last revised 17 Mar 2022 (v4)

HAL is a multi-disciplinary open access archive for the deposit and dissemination of scientific research documents, whether they are published or not. The documents may come from teaching and research institutions in France or abroad, or from public or private research centers.

L'archive ouverte pluridisciplinaire **HAL**, est destinée au dépôt et à la diffusion de documents scientifiques de niveau recherche, publiés ou non, émanant des établissements d'enseignement et de recherche français ou étrangers, des laboratoires publics ou privés.

Optimal multiple motion encoding in Phase-Contrast MRI

Helge Herthum¹, Hugo Carrillo², Axel Osses², Sergio Uribe³, Ingolf Sack¹, Cristóbal Bertoglio⁴

¹Department of Radiology, Charité - Universitätsmedizin Berlin, Berlin, Germany

²Center for Mathematical Modeling, Universidad de Chile, Santiago, 8370456, Chile

³Biomedical Imaging Center, Pontificia Universidad Católica de Chile, Santiago, 7820436, Chile

⁴Bernoulli Institute, University of Groningen, Groningen, 9747AG, The Netherlands

September 23, 2020

Abstract

Purpose: To propose an optimal multiple motion encoding (OMME) method for Phase-Contrast MRI (PC-MRI) with application to Magnetic Resonance Elastography (MRE) for reconstructing wrap-free wave images.

Theory: OMME is formulated and analyzed as an extension of [5] using an arbitrary number of measurements with different motion encoding gradients (MEG) to increase the dynamic range of motion encoding.

Methods: OMME is assessed numerically for several high and low motion sensitivity ratios in terms of *motion-to-noise-ratio* (MNR) for different image SNR. The algorithms are then tested on MRE data from heparin phantom experiments and ultimately from in vivo human brain experiments for the most robust MEGs combination. The wrap-free motion images are further used to reconstruct shear wave speed (SWS) maps and compared to the ones obtained using conventional phase unwrapping methods.

Results: For the dual encoding case, OMME performs better than the standard method, in terms of robustness to noise and effective MNR. OMME allowed to successfully combine three and four MRE wave images with different dynamic ranges in the phantom and volunteer data, respectively, leading to SWS maps which preserve important details (e.g. discontinuities in the stiffness) when compared to conventional unwrapping methods.

Conclusion: In Phase-Contrast MRI, with OMME the MNR grows exponentially with the number of measurements as opposed to standard image averaging. In MRE, this allows for great improvements in recovering tissue details in the SWS maps in contrast to conventional unwrapping methods.

1 Introduction

Phase-Contrast MRI (PC-MRI) is a well-established method for measuring flow velocities [26] or tissue displacements due to harmonic excitation as used in Magnetic Resonance Elastography (MRE) [10, 16, 14, 25, 11, 19].

Motion is encoded in the phase of the complex transverse magnetization proportional to the encoding efficiency of the motion encoding gradient (MEG). However, the phase can only be measured in the half-open interval $[-\pi, \pi)$ and phase wraps (abrupt jumps of $\pm 2\pi$) occur if the encoded phase exceeds those limits. Hence for a given encoding efficiency, there is a fixed amplitude range or *dynamic range*, where motion can be acquired without phase wraps. If the encoding efficiency is too large and the true motion amplitude exceeds the dynamic range, phase wraps occur. Unfortunately, selecting a large dynamic range leads to poor quality images since for a given signal-to-noise-ratio (SNR) in the magnitude image, the “motion-to-noise-ratio” (MNR) is proportional to the dynamic range.

Phase wrapping is one of the main limitations for measuring complex features of blood flows, particularly, when high and low velocities are present in the same image, such as in heart, valvular and vascular malformations [4]. In MRE, the induced mechanical waves are prone to frequency dependent damping which leads to possibly large spatial variations in the displacement magnitude towards the interior of the organs. There are usually two approaches to generate wrap-free phase images.

First, unwrapping algorithms have been developed by assuming that the motion field is smooth in space, see e.g. [13] for flow MRI and [2] for MRE, and references therein. Nevertheless, they can not recover the true underlying motion for various reasons and fail when the aliased regions are complex, subject to noise or include nested wraps. In such cases the unwrapped phase appears to be distorted and obstructs further data processing steps. For instance, the simple 2π -unwrapping Flynn [9] algorithm is inherently two-dimensional and fails to unwrap noisy complex wraps when no well-defined enclosed region exists. The true motion can not be recovered because arbitrary 2π -offsets are added. Gradient based algorithms [20] only yield the derivative of the phase and amplify noise. Laplacian based unwrapping algorithms [22] remove the constant and linear terms from the data and induce spatial smoothing. The resulting phase is altered and important details may be lost.

Second, voxelwise motion reconstructions using dual-encoding strategies have been proposed in PC-MRI which are based on unwrapping low dynamic range data by using the high dynamic range data. In other words, the goal is to include additional measurements with a reduced dynamic range (hence, improved MNR) while maintaining a large dynamic range for the reconstructed image. Those methods do not involve any assumption of smoothness of the motion-encoded phase field [12, 21, 5, 30] as an alternative to avoid altering the output motion image but at the price of additional measurements. To the best of the authors’ knowledge, there is neither any reported analysis of their performance with respect to SNR of dual encoding nor an extension to multiple encoding.

Hence, the aim of this work is threefold.

Firstly, to mathematically and numerically analyze dual-encoding strategies as a way to answer the question: Which combination of MEGs provides the best MNR for a given dynamic range (number of phase wraps) and SNR? As a conclusion, it will be shown that the so-called *optimal dual-encoding* [5] shows the best performance in terms of noise robustness for dual encoding, while providing a mathematical framework to select an optimal set of MEGs.

Secondly, we will show how the optimal dual-encoding approach provides a straightforward extension to multiple motion encoding, the Optimal Multiple Motion Encoding (OMME) method.

And thirdly, it will be shown that OMME can successfully provide wrap-free low dynamic range MRE phase images for phantom and in vivo brain experiments which are closest to the true

underlying motion in the range of the MNR of the smallest dynamic range. Reconstructed wrap-free phase images are used as input for MRE reconstruction and allow to recover more details in the SWS maps compared to common phase-unwrapped input images.

2 Theory

This section deals with the mathematical framework of the work and it is therefore general for any PC modality.

2.1 Single motion-encoding in PC-MRI

For a given MEG G , the model of measured phase can be written in the form

$$\varphi_G(u) = \varphi_0 + \delta_G + u \frac{\pi}{d_G} + \varepsilon\pi \quad (1)$$

with the following notation:

- φ_0 is the reference phase due to the static field inhomogeneities,
- δ_G is a MEG-dependent phase induced e.g by eddy currents and Maxwell effects,
- d_G is the “dynamic range”, i.e. the inverse of the encoding efficiency depending on the MEG’s amplitude, duration, time shape and alignment with the mechanical wave, or the *vinc* parameter in flow MRI,
- u denotes the tissue harmonic displacement or flow velocity in the direction of the MEG, for MRE or Flow MRI, respectively.
- $\varepsilon \sim \mathcal{N}(0, \sigma_\varphi^2)$ represents the measurement noise in the phase. The value of σ_φ^2 depends on the SNR of the magnitude measurements.

We will also denote u_{true} the ground truth displacement/velocity.

In the case of MRE, the motion u is usually recovered by either:

1. Measuring φ_G using a MEG at equidistant timepoints of one cycle of the propagating mechanical wave, and then only use the first harmonic component using time-frequency domain analysis to remove stationary and higher harmonic components, or
2. Obtaining one (single time point) measurement without any vibration but with the MEG turned off to measure $\varphi_G(0) = \varphi_0 + \delta_G + \varepsilon\pi$. Then such measurement is repeated with the mechanical vibration on to measure $\varphi_G(u)$ for the all other time steps. Since usually the number of time steps measured are at least 4 (but typically 8), the additional measurement of $\varphi_G(0)$ involves a negligible scan time.

Notice that we have neglected the phase encoded by imaging gradients, but this contribution can be neglected since those gradients are usually velocity compensated and only higher order terms contribute.

If $\varphi_G(0)$ is directly measured, u can be computed as:

$$u = (\varphi_G(u) - \varphi_G(0)) \frac{d_G}{\pi} - (\varepsilon_u - \varepsilon_0) d_G \quad (2)$$

with ε_u and ε_0 independent realizations of ε for the both phase measurements. As a consequence, $u \sim \mathcal{N}(\bar{u}, 2d_G^2\sigma_\varphi^2)$ since at least two phase measurements are needed due to the unknowns u and $\varphi_G(0)$. Therefore, d_G should be chosen as small as possible.

However, phase can be measured only within the interval $[-\pi, \pi)$. Hence, if $d_G < |u_{true}|$ (if $\sigma_\varphi = 0$) then the measured displacement u wraps by a multiple of $2d_G$. Naturally, aliasing can occur even if $d_G > |u_{true}|$ in the presence of noise $\varepsilon \neq 0$.

For a given dynamic range, a natural approach to reduce the variance of u is to average more measurements. If n is the number of measurements made of φ_G (always with the same d_G) and n_0 the number of measurements of $\varphi_G(0)$, then

$$u \sim \mathcal{N}(\bar{u}, d_G^2\sigma_\varphi^2(n^{-1} + n_0^{-1})) = \begin{cases} \mathcal{N}(\bar{u}, \left(\frac{d_G}{\sqrt{n}}\right)^2 \sigma_\varphi^2), & n \ll n_0 \\ \mathcal{N}(\bar{u}, 2\left(\frac{d_G}{\sqrt{n}}\right)^2 \sigma_\varphi^2), & n = n_0 \end{cases} \quad (3)$$

From this relation it is clear that decreasing d_G is more effective than increasing the number of measurements n , since the standard deviation of u decreases linearly with respect to d_G/\sqrt{n} .

2.2 Classical dual motion encoding revisited

The goal of multiple motion encoding approaches is to include additional measurements with a reduced value of d_G (e.g., larger MEGs) while maintaining the dynamic range of the motion image large. In this section we will treat the case of dual encoding, i.e. for two different values d_1, d_2 for d_G .

We assume now that we measure phases with two different MEGs amplitudes $G_1 < G_2 = G_1/\beta$, with $0 < \beta < 1$. This results in four measured phases $\varphi_1, \varphi_1(0), \varphi_2, \varphi_2(0) \sim \mathcal{N}(0, \sigma_\varphi^2)$. In the case $\sigma_\varphi = 0$, these phases satisfy the relations:

$$\varphi_1 = \varphi_1(0) + u \frac{\pi}{d_1}, \quad \varphi_2 = \varphi_2(0) + u \frac{\pi}{d_2}.$$

From the noisy measurements, four motion images can be reconstructed:

$$u_1 = \frac{\varphi_1 - \varphi_1(0)}{\pi} d_1, \quad u_2 = \frac{\varphi_2 - \varphi_2(0)}{\pi} d_2, \quad u_{ps} = \frac{\varphi_1 + \varphi_2 - \varphi_1(0) - \varphi_2(0)}{\pi} d_{ps}, \quad u_{pc} = \frac{\varphi_2 - \varphi_1 + \varphi_1(0) - \varphi_2(0)}{\pi} d_{pc}$$

with $d_{ps} = (d_1^{-1} + d_2^{-1})^{-1}$, $d_{pc} = (d_2^{-1} - d_1^{-1})^{-1}$. Notice that

$$d_{pc} = d_1 \frac{\beta}{1 - \beta} \geq d_1 > d_2 = \beta d_1 > d_{ps} = d_1 \frac{\beta}{1 + \beta}.$$

and therefore we call $d_{pc} = d_{eff}$ as the *effective dynamic range* of the dual encoding method. In case $\sigma_\varphi > 0$, the variances of the different motion estimators satisfy:

$$\text{Var}(u_{pc}) > \text{Var}(u_1) > \text{Var}(u_2) > \text{Var}(u_{ps})$$

and by defining $\alpha = \sqrt{2}\sigma_\varphi d_1$, more precisely we have

$$\text{Var}(u_{pc}) = 4\sigma_\varphi^2 d_{pc}^2 = \alpha^2 \frac{2\beta^2}{(1 - \beta)^2} = \alpha^2 \frac{\beta^2}{\left(\frac{1 - \beta}{\sqrt{2}}\right)^2}, \quad \text{Var}(u_1) = 2\sigma_\varphi^2 d_1^2 = \alpha^2,$$

$$\text{Var}(u_2) = 2\sigma_\varphi^2 d_2^2 = \alpha^2 \beta^2, \quad \text{Var}(u_{ps}) = 4\sigma_\varphi^2 d_{ps}^2 = \alpha^2 \frac{2\beta^2}{(1+\beta)^2} = \alpha^2 \frac{\beta^2}{\left(\frac{1+\beta}{\sqrt{2}}\right)^2}.$$

Dual encoding reconstructions aim to unwrap a motion reconstructed with low dynamic range using a motion reconstructed with a high dynamic range as follows [12]:

$$u_{uw} = u_{low} + 2d_{low} N.I. \left(\frac{u_{high} - u_{low}}{2d_{low}} \right) \quad (4)$$

with $N.I.$ the nearest integer operator. This leads to $\text{Var}(u_{uw}) = \text{Var}(u_2)$ when the unwrapping is successful. This method will be denoted in as *standard dual encoding*. To pick up u_{low} and u_{high} we apply the following reasoning. Firstly, we pick $u_{low} = u_2$ since it possess a higher dynamic range than u_{ps} (e.g. $d_{pc} = 3/2d_{ps}$ for $\beta = 1/2$) only with a slightly higher variance (e.g. $\text{Var}(u_2)/\text{Var}(u_{ps}) = 1.125$ for $\beta = 1/2$). Secondly, we pick

$$u_{high} = \begin{cases} u_1 & \beta \in \{1/2, 1\} \\ u_{pc} & \text{elsewise} \end{cases}$$

since u_{pc} has the desired effective range $d_{eff} \geq d_1$, but for $\beta = 1/2$ it holds $d_1 = d_{eff}$ and $\text{Var}(u_1) < \text{Var}(u_{pc})$, and for $\beta = 1$ u_{pc} is not defined and $d_1 = d_{eff}$.

2.3 The optimal dual motion encoding method revisited [5]

In [5], a new method for unwrapping two motion-encoded images was introduced, the so called *Optimal dual venc* (ODV) method (since it was originally propose for flow MRI). In the next lines we will recall the method, and show some new theoretical results.

The method is based on the formulation of the phase contrast problem as the minimization of cost functional. For the single motion encoding case, the cost functional has the form:

$$J_i(u) = 1 - \cos\left(\varphi_i - \varphi_G(0) - \frac{\pi u}{d_i}\right) = 1 - \cos\left(\frac{\pi}{d_i}(u_i - u)\right)$$

which comes from a least squares approximation for the angle by measuring the components of a vector and where φ_i and $\varphi_G(0)$ where defined in the previous section.

It is easy to prove that the minima of $J(u)$ correspond to the classical PC formula and therefore the periodicity of $J_i(u)$ is $2d_i$. The single encoding PC motion is the smallest value (in absolute terms) where the minima is attained.

For the dual encoding case, the problem shifts from finding the local minima of $J(u)$ to find the global minima of

$$J_{dual}(u) = J_1(u) + J_2(u) = 2 - \cos\left(\frac{\pi}{d_1}(u_1 - u)\right) - \cos\left(\frac{\pi}{d_2}(u_2 - u)\right)$$

It was proven in [5] that u_{true} is a global minimum of J_{dual} . Moreover, as a new result, J_{dual} has periodicity $2d_{eff}$ when $\beta = n/(n+1)$, $n \in \mathbb{N}$. Indeed:

$$J_{dual}(u + 2d_{eff}) = 2 - \cos\left(\frac{\pi}{d_1}\left(u_1 - u - 2\frac{d_1\beta}{1-\beta}\right)\right) - \cos\left(\frac{\pi}{d_2}\left(u_2 - u - 2\frac{d_1\beta}{1-\beta}\right)\right) \quad (5)$$

$$= 2 - \cos\left(\frac{\pi}{d_1}(u_1 - u) - 2\pi n\right) - \cos\left(\frac{\pi}{d_2}(u_2 - u) - 2\pi(n+1)\right) = J_{dual}(u) \quad (6)$$

In the optimal dual encoding method, the unwrapped motion corresponds then to the global minimum with smallest magnitude, which we will call u_* . Therefore, due to the $2d_{eff}$ -periodicity, aliasing will occur when $d_{eff} \leq |u_{true}|$. Notice that in opposite than the standard dual veng for $\beta \neq 1/2$ we do not need u_{pc} for unwrapping: both u_1 and u_2 can be aliased, still resulting in an unwrapped u_* .

In [5], no theoretical noise analysis was performed, which will be therefore shown here. First, we need an expression u_* , which can be obtained from the fact that the global minimum is also a local minimum, i.e. $J'_{dual}(u_*) = 0$. Indeed

$$\begin{aligned} J'_{dual}(u_*) &= -\frac{\pi}{d_1} \sin\left(\frac{\pi}{d_1}(u_1 - u_*)\right) - \frac{\pi}{d_2} \sin\left(\frac{\pi}{d_2}(u_2 - u_*)\right) \\ &= -\frac{\pi}{d_1} \sin\left(\frac{\pi}{d_1}(u_1 + 2k_1d_1 - u_*)\right) - \frac{\pi}{d_2} \sin\left(\frac{\pi}{d_2}(u_2 + 2k_2d_2 - u_*)\right) \end{aligned}$$

for all $k_1, k_2 \in \mathbb{Z}$. Notice that $u_* \approx u_1 + 2k_1d_1 \approx u_2 + 2k_2d_2$ for some fixed k_1, k_2 in case of small measurement noise in the phase (and equal if no noise is present). Therefore, we can approximate the sin-terms by its arguments leading to:

$$u_* \approx (d_1^{-2} + d_2^{-2})^{-1} (u_1d_1^{-2} + u_2d_2^{-2} + 2(k_1d_1^{-1} + k_2d_2^{-1})). \quad (8)$$

Since assume all that measurements are statistically independent (and therefore u_1 and u_2), the variance of u_* has the form

$$\text{Var}(u_*) = (d_1^{-2} + d_2^{-2})^{-2} (\text{Var}(u_1)d_1^{-4} + \text{Var}(u_2)d_2^{-4}) \quad (9)$$

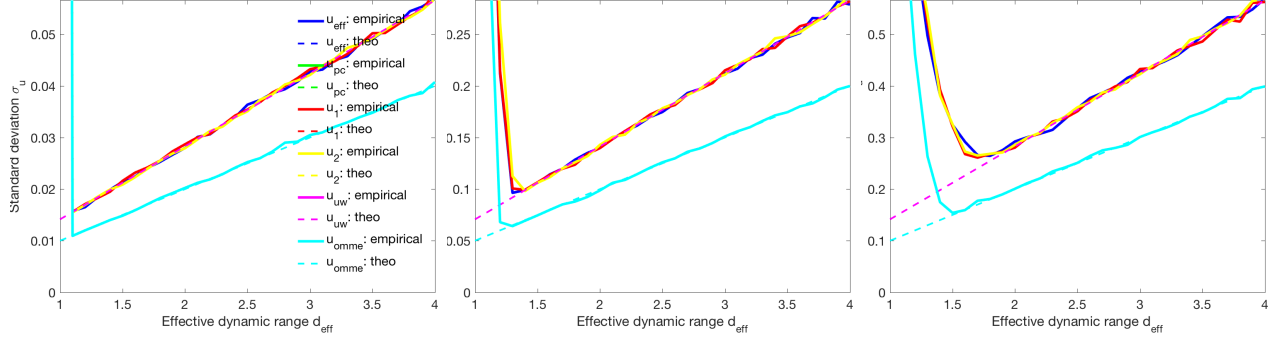
$$= (d_1^{-2} + d_2^{-2})^{-2} (\alpha^2d_1^{-4} + \alpha^2\beta^2d_2^{-4}) = \frac{\text{Var}(u_2)}{1 + \beta^2} < \text{Var}(u_2). \quad (10)$$

And therefore an improved estimate in terms of variance is obtained.

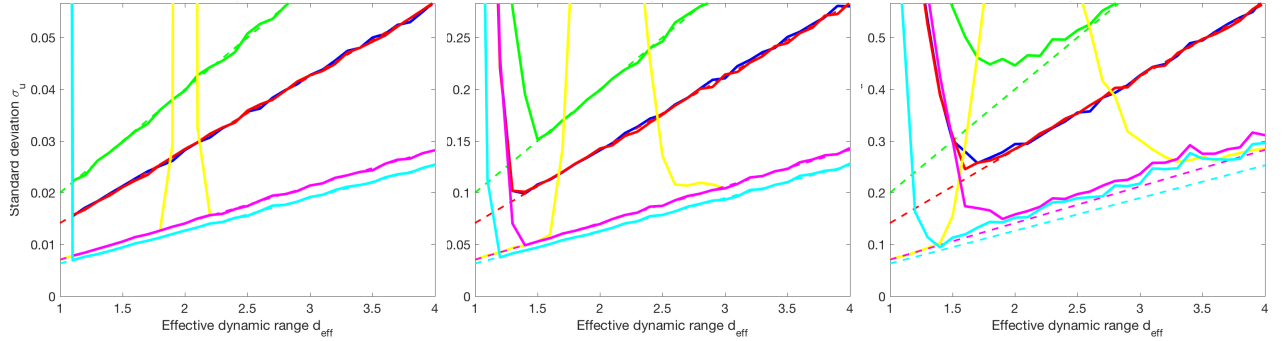
Figure 1 presents the previous findings in a graphical way. There, we show the standard deviations of the estimators (i.e. the square root of the variances) versus the effective dynamic ranges for various values of β . The plots are constructed as follows:

- For a fixed value of d_{eff} and β , d_1 and d_2 are computed and 5000 realizations of the measurements for all four phases are generated using a value for σ_φ . Here, the ground truth values are $\bar{u} = 1$ and $\varphi_1(0) = \phi_0$ and $\varphi_2(0) = 2\phi_0$, with $\phi_0 = 0.9\pi$.
- Then u_1, u_2, u_{uv}, u_* are computed. Also u_{eff} being the single motion phase contrast estimate with $d_G = d_{eff}$ is computed for comparison.
- The standard deviation of such estimates considering the 5000 realizations is computed.
- The curves are drawn by repeating this procedure in the interval $d_{eff} \in [1, \dots, 4]$.
- Four values of $\beta \in \{1, 1/2, 2/3, 3/4\}$ are used. The value $\beta = 1$ means that two set of measurements are obtained with the same dynamic range. This serves for better assessing the gains of dual encoding approaches.

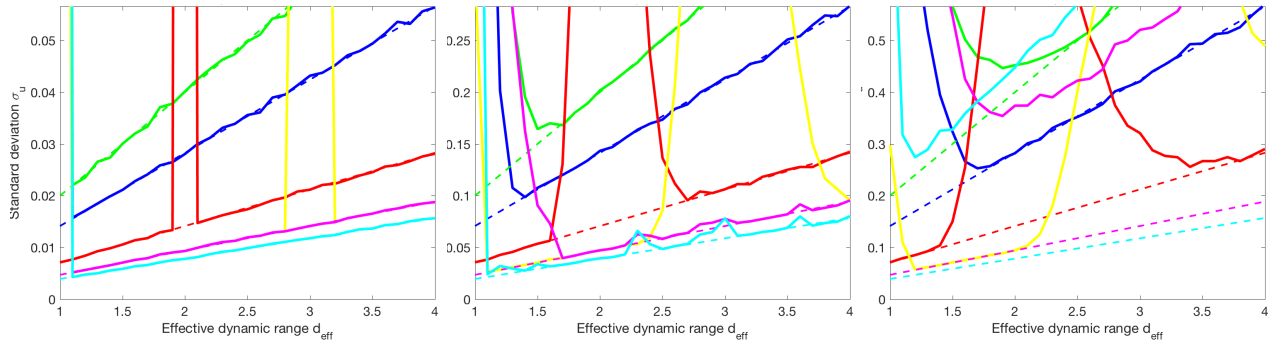
First note that the peaks in the empirical curves come from aliasing for the corresponding dynamic range, and the larger σ_φ the larger the interval where aliasing may occur.



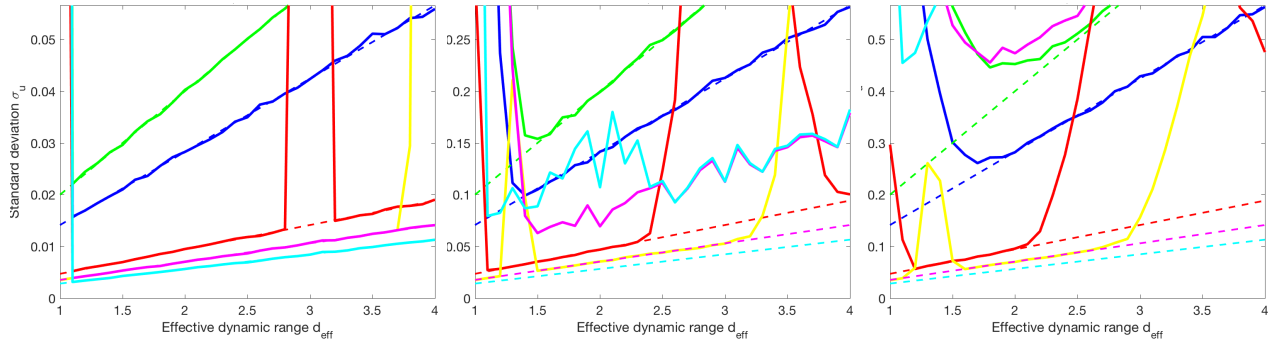
(a) $\beta = 1$. The curve for u_{pc} is not shown since it is not defined. All curves lie on each other except in the optimal method. The region of aliasing becomes larger when increasing σ_φ .



(b) $\beta = 0.5$. Aliasing occurs for u_2 at $d_{eff} = 2$, as expected. All other cases have aliasing limit at $d_{eff} = 1$.



(c) $\beta = 2/3$. Aliasing occurs for u_1 at $d_{eff} = 2$ and for u_2 at $d_{eff} = 3$, as expected.



(d) $\beta = 3/4$. Aliasing occurs for u_1 at $d_{eff} = 3$ and for u_2 at $d_{eff} = 4$, as expected. For this value of β , results become very sensitive to noise.

Figure 1: Single v/s dual motion encoding in one voxel. Left column: $\sigma_\varphi = 0.01$. Middle column: $\sigma_\varphi = 0.05$. Right column: $\sigma_\varphi = 0.1$. The continuous lines represent the empirical variances and (i.e. the one computed from the numerical experiments) and the dashed lines the theoretical ones derived before.

The quality of the results depends on both values of β and σ_φ . For small values of σ_φ , the empirical and theoretical standard deviations match, but the empirical deviates from the theoretical one when $d_{eff} \rightarrow |u_{true}|$, as expected, due to the aliasing. In this low noise scenario, the maximum gain with respect to the case of repeating the same measurements (i.e. $\beta = 1$) is when $\beta = 3/4$ since for a fixed d_{eff} , $d_1 = d_{eff}/3$ and $d_2 = d_{eff}/4$.

However, the reconstruction with $\beta = 3/4$ becomes unrobust when increasing σ_φ . The most robust variant with respect to noise for both standard and optimal methods appears to be $\beta = 1/2$, where $d_1 = d_{eff}$ and $d_2 = d_{eff}/2$. In case of the optimal method, this can be explained by the fact that the local minima of both J_1 and J_2 cost functionals have maximal distance. For $\beta = 3/4$, this distance is much smaller, see details in [5].

In particular for $\beta = 1/2$, among both methods, the optimal dual encoding appears to be more robust with respect to noise, specially when $d_{eff} \rightarrow |u_{true}|$, and slightly better than the standard dual encoding approach when $d_{eff} > |u_{true}|$ due to (9). The possible explanation is that unwrapping and noise compensation are done simultaneously, and therefore, a more robust unwrapping method results.

In conclusion, we adopt from now on $\beta = 1/2$. This choice makes the formulation of a multiple encoding reconstruction easy to implement and analyze. Moreover, it has the practical advantage that at least one image with the desired d_{eff} is acquired, what can be convenient in case e.g. of uncooperative patients.

2.4 Optimal multiple motion encoding (OMME)

The optimal dual encoding formulation allows a straightforward extension to multiple MEGs, i.e.

$$J_N(u) = \sum_{j=1}^N \left(1 - \cos \left(\frac{\pi}{d_j} (u_j - u) \right) \right)$$

The multiple motion encoding reconstruction u_* is then the global minimum of smallest magnitude.

Analogously to the dual encoding case, the optimum can be found to approximately be

$$u_* \approx \left(\sum_{j=1}^N d_j^{-2} \right)^{-1} \left(\sum_{j=1}^N u_j d_j^{-2} + 2k_j d_j^{-1} \right), \quad k_j \in \mathbb{Z}, \quad j = 1, \dots, N$$

with variance

$$\begin{aligned} \text{Var}(u_*) &= \left(\sum_{j=1}^N d_j^{-2} \right)^{-2} \sum_{j=1}^N \text{Var}(u_j) d_j^{-4} = 2\sigma_\varphi^2 \left(\sum_{j=1}^N d_j^{-2} \right)^{-2} \sum_{j=1}^N d_j^{-2} \\ &= 2\sigma_\varphi^2 \left(\sum_{j=1}^N d_j^{-2} \right)^{-1} = \text{Var}(u_N) \left(\sum_{j=1}^N \left(\frac{d_N}{d_j} \right)^2 \right)^{-1} < \text{Var}(u_N) \end{aligned}$$

If we consider the case $d_N = d_j \beta^{N-j}$ for $j = 1, \dots, N$, we obtain:

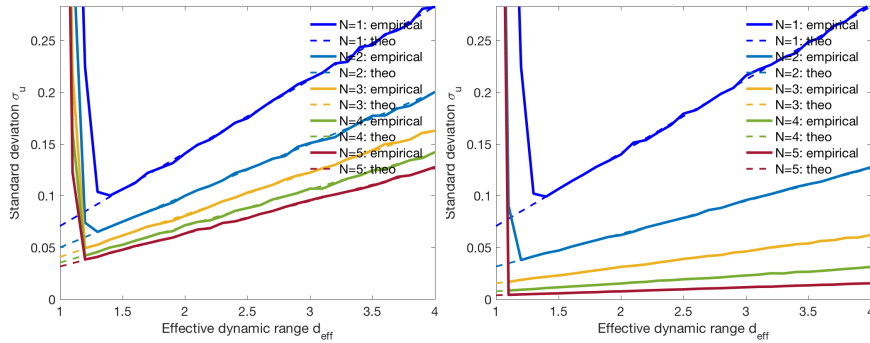
$$\text{Var}(u_*) = \text{Var}(u_N) \beta^{-2N} \left(\sum_{j=1}^N \beta^{-2j} \right)^{-1} = \text{Var}(u_N) \frac{1 - \beta^2}{1 - \beta^{2N}} = \text{Var}(u_1) \beta^{2(N-1)} \frac{1 - \beta^2}{1 - \beta^{2N}}.$$

Notice the exponential reduction of the standard deviation with respect to the number of measurements, instead of linear which is the case when averaging of equal dynamic range data (i.e. $\beta = 1$).

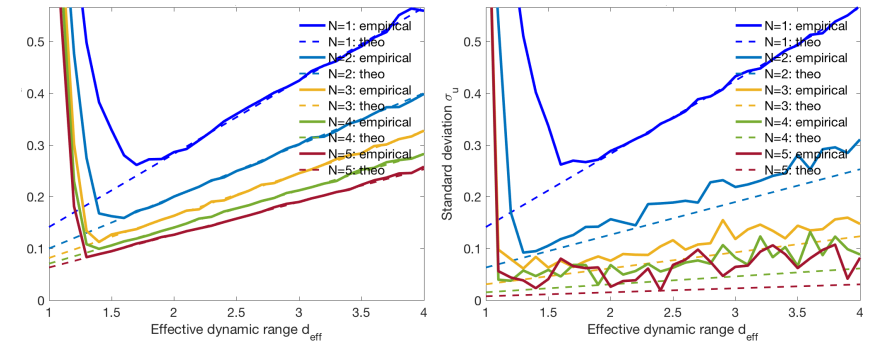
Figure 2 shows the results for the standard deviation versus d_{eff} for the case of $\beta = \{1/2, 1\}$ and $N = 1, \dots, 5$.

For large noise, i.e. $\sigma_\varphi = 0.1$, the empirical standard deviations deviate from the theoretical ones, most likely due to failure in unwrapping due to the noise. This is a relevant aspect and implies in practice that noise limits escalation of multiple encoding to an arbitrary number of MEGs. Therefore, if noise becomes stronger, simple averaging will become the most robust alternative for noise reduction in the motion image.

The theoretical calculations are confirmed and in the case $\sigma_\varphi = 0.05$ the large superiority of the multiple encoding approach (right, $\beta = 0.5$) compared to averaging (left, $\beta = 1$) in terms of noise reduction can be observed. Indeed, it takes 5 averages to achieve the same standard deviation in the motion that only multiple encoding measurements.



(a) $\sigma_\varphi = 0.05$. Left: $\beta = 1$. Right: $\beta = 1/2$.



(b) $\sigma_\varphi = 0.1$. Left: $\beta = 1$. Right: $\beta = 1/2$.

Figure 2: Multiple motion encoding reconstruction. The continuous lines represent the empirical variances and (i.e. the one computed from the numerical experiments) and the dashed lines the theoretical ones.

3 Methods

3.1 Phantom experiments

Phantom tests were performed using heparin-sodium gel (180 000 IU per 100 g, Ratiopharm, Ulm, Germany) in a 2 L cubic container to confirm the behaviour described in the theory on experimental MRE data. The gel mainly consists of Carbomer 980 (polyacrylic acid), trometamol (TRIS), glycerol hydroxystearate, propylene glycol, and isopropanol with the eponymous active agent only accounting for less than 1% of the gel volume. All experiments were performed in a 3.0T MRI scanner (Siemens Magnetom Lumina, Erlangen, Germany).

In the phantom some air inclusions appeared which allow to assess the capacity of the reconstruction methods to resolve image details.

External harmonic vibrations at 30.03 Hz were induced by a pressurized air driver operating at 150 mBar as described elsewhere [23]. The driver was acting on a plate vertically immersed in the gel to reduce vibrations of the casing and to provide plane wave propagation in mainly one direction. The setup is shown in Figure 3. The vibrations were induced 2 s before data acquisition started to ensure a steady state of time-harmonic oscillations of the medium. The wave generator [6] was synchronized with the MRI clock to ensure optimal timing for data acquisition [29].

One component of the wavefield in top-bottom direction was acquired by using a single-shot, spin-echo echo-planar imaging sequence with flow-compensated MEGs. Eight phase offsets over a full vibration period were recorded at 10 consecutive centered coronal slices with a field-of-view of $130 \times 160 \text{ mm}^2$ and $1.27 \times 1.27 \times 0.9 \text{ mm}^3$ voxel size. Further imaging parameters were: echo time = 165 ms; repetition time = 2500 ms; flip angle 90° ; MEG frequency of 29.45 Hz and MEG amplitude of {2, 4, 8,16,32} mT/m respectively. The experiment was repeated without external vibrations to measure $\varphi_G(0)$ (see Section 2).

Notice that this is different from the phase measured with external vibrations on and MEG amplitude of 0 mT/m. In the first case (Vibration off, MEG on) the phase offset is induced by the eddy currents of the MEGs and any other residual motion encoded by the MEGs. Small temporal variations due to residual tissue motion can be neglected and only one time step per encoding directions needs to be measured. In the other case (Vibration on, MEG off) motion induced phase variations encoded by the imaging gradients are measured. Here it is sufficient to measure only one encoding direction, but all time steps are necessary. We found that the MEG induced phase offset is much stronger than phase offsets due to motion encoding by the imaging gradients. Therefore we chose vibration off and MEG on in order to measure the offset phase.

3.2 Volunteers

In vivo MRE was performed in 1 healthy volunteer (male, age 29). The study was approved by the ethics committee of Charite Universitaetsmedizin Berlin in accordance with the Ethical Principles for Medical Research Involving Human Subjects of the World Medical Association Declaration of Helsinki. The participant gave written informed consent. External harmonic vibrations at 25 Hz were introduced by two pressurized air drivers at 650 mBar. The drivers were placed under the volunteers head and operated in alternate fashion similar to [23].

Three components of the wavefield in orthogonal directions were acquired without flow-compensated MEGs. Eight phase offsets over a full vibration period were recorded at 11 transversal slices (50% slice gap) with a field-of-view of $200 \times 200 \text{ mm}^2$ and $2 \times 2 \times 2 \text{ mm}^3$ voxel size. Further imaging

parameters were: echo time = 81 ms; repetition time = 1750 ms; flip angle 80 deg; MEG frequency of 27.75 Hz and MEG amplitude of {2, 4, 8, 16, 32} mT/m respectively. Again the experiment was repeated without external vibrations to measure $\varphi_G(0)$. Acquisition time (TA) for the measurement with one MEG amplitude is 42 s (for all three encoding directions), plus the acquisition of the respective offset phase which takes 5.25 s. For the conventional MRE data processing, where the phase unwrapping is done using phase unwrapping algorithms and the offset phase is removed by the temporal Fourier transform, a single acquisition of 42 s suffices.

3.3 MRE data processing

3.3.1 Wave images

Single encoding-phase contrast wave images were computed for each MEG using Equation (2) (assuming no noise). Dual encoding wave images were computed using combinations of those single encoding images using standard and optimal methods. Also, OMME was used to combine wave images with several MEGs. The specific chosen MEGs are indicated in each figure in the results section. Wrapped single motion encoding phase images were unwrapped using Laplacian and Flynn based unwrapping algorithm as outlined in the introduction.

Moreover, in the phantom we compute additional wave images by adding a random noise to the measured phase with $\varphi = 0.1$, since the original data was estimated to have $\varphi = 0.02$.

3.3.2 Shear wave speed reconstruction

Finally, the wrap-free phase images from the single and multiple encoding methods were used for reconstruction of SWS maps based on single-gradient wavenumber recovery to avoid noise amplification of the Laplacian, which is invoked by direct inversion techniques [10, 18]. SWS is related to tissue stiffness. The principle of wavenumber (k-) based multi-component, elasto-visco (k-MDEV) inversion was originally introduced for liver MRE and is outlined in [28]. First the complex MRE data is smoothed using a Gaussian filter and then unwrapped (Laplacian). The unwrapped phase images are temporally Fourier transformed and the first harmonic component is selected and denoted as wavefield. For further data processing the wavefield is Fourier transformed into the spatial domain (2D) and multiplied with a radially increasing linear filter function to suppress compression waves. Next, the filtered wavefield is decomposed into eight propagation directions. To do so, the wavefield is subjected to a directional filter with increasing angle and each filtered wavefield is transformed back to image space. These images contain propagating waves with approximately a single propagation direction. This fulfils the underlying assumptions of the final k-MDEV inversion, where the wavenumber is determined from the phase gradient and subsequently transformed to a propagation velocity or SWS. k-MDEV inversion was never applied to brain MRE data before. Therefore we had to adapt the spatial filters used in the post processing to match the different resolutions and wave patterns encountered in brain MRE data in order to avoid over-smoothing and better resolve the brain anatomy. The actual inversion step was left unchanged. First the smooth of the complex signal prior to the temporal Fourier transform was removed and secondly the linear radial filter in the spatial frequency domain was replaced by a radial bandpass Butterworth filter with highpass threshold of 15 1/m (order 3) and lowpass threshold of 350 1/m (order 3, phantom data) and 200 1/m (order 3, in vivo data). Different lowpass threshold values for the phantom and in vivo data were chosen due to different spatial resolution and therefore different extend of the spatial frequency domain. We moved the smoothing (lowpass filter) to a

later point because the directional filter induces high frequency noise which otherwise can not be suppressed. In fact it removes conjugate spatial frequencies to separate waves propagating into opposed directions. This also removes high spatial frequency components associated with noise which previously leaked across the spectrum which results in high frequency noise in the filtered wavefields across the whole image.

3.3.3 Noise analysis

Signal intensity and noise level of the wrap-free wavefields are important parameters for the subsequent post-processing and final SWS reconstruction. OMME promises to deliver low noise (high MEG), wrap-free images with the noise level given by the highest MEG used in the OMME phase recovery. To calculate the noise levels for experimental data we used the blind noise estimation method of Donoho et al. [7] as outlined and previously applied to MRE data in [3]. Noise estimation in the wavelet domain is expected to be well suited for wave images [1, 24]. Recent work [17, 15] suggests using the SNR of the derivative images rather than the displacement images as a determinant of the image quality, as the numerical derivative have an dominant effect on the SWS recovery. Therefore we estimated the noise levels from the dual-tree wavelet transformation of the Laplacian image with the median absolute deviation of the finest band of wavelet coefficients [7]. The estimated signal power is derived from the L2-norm. Levels are estimated in a central region of the wavefield (see Figure 3i and Figure 9m) for all slices and components and averaged afterwards.

4 Results

4.1 Experimental phantom

Figure 3 presents the reconstructions for the single encoding cases, optimal and standard dual encoding, and OMME using three MEGs. Results are as expected, i.e. both dual encoding methods show the wraps of the low MEG image. The standard and dual encoding methods behave similarly, since $\beta = 1/2$ and the noise level of the images is low $\sigma_\varphi \approx 0.02$, which is estimated from MEG=0 images. The tri-MEG image shows also the dynamic range of the largest MEG. All dual and tri MEG including MEG=8 are fully unwrapped. Figure 4 presents the same reconstructions but colored in a smaller motion range, in order to put in evidence the gain in the MNR when increasing the number of gradients within OMME in the regions with low motion amplitude, i.e. far from the vibration probe (left part of the pictures).

The reconstructions with additional random noise to the measured phase with $\varphi = 0.1$ are shown in Figure 5. Now, differences between standard and optimal dual encodings are perceptible, appearing the optimal method to be more robust as it was shown in Figure 1b in the numerical simulations. It is also now more evident how the tri-MEG optimal variant strongly increases the MNR of the image.

Finally, we present in Figure 6 the resulting SWS maps from the single and optimal multiple encoding reconstructions, and compared with Laplace and Flynn unwrapping on the single encoding images. It can be appreciate that in all cases the SWS maps are more homogeneous towards the center of the phantom and more noise far from the probe, as expected since the wave is damped with decreasing the MNR. However, it is also clear that increasing the MEG reduces the noise in the SWS maps in all cases. Both conventional phase unwrapping algorithms exhibit different drawbacks. Laplacian based unwrapping smooths image details as it can be seen from the disappeared air

inclusions in the reconstructed SWS map for the phantom data. In the case of Flynn the inclusions disappear as well but for a different reason: at the air-heparin boundary a phase jump occurs but not of magnitude $\pm 2\pi$ and therefore Flynn is unable to recover the true motion and the reconstruction fails.

Moreover, this smoothing effect seems to be more important when the MEG increases, probably due to the fact that more wraps appear in the wave image amplifying the smoothing effects of the unwrapping algorithm. Flynn gets more unstable the more wraps occur. In contrast, OMME allows to recover both image details, without wraps and obtaining a smoother SWS map, what is expected in this case since the material is the same everywhere in the phantom.

4.2 Volunteers

In Figure 7 and 8 we present the wavefields and reconstructed SWS maps for the in vivo brain experiment. In this case, we combined four MEGs with OMME to fully omit standard unwrapping procedures. Compared are SWS reconstructions based on wrap-free phase images from OMME, Laplacian based unwrapping and Flynn unwrapping.

In particular, while some details are smoothed but still present when applying Laplace and Flynn (in green), OMME allows to preserve more details in the resulting SWS map. Especially tissue/air boundaries are better preserved and noise outside the brain is heavily reduced. In general the contrast of the image is better with OMME.

In this example the capability of OMME to compensate for wraps and noise simultaneously becomes evident. Note in Figure 7a that in the lower part wraps are still present for the lowest MEG. As expected, the standard dual MEG method cannot unwrap it, see Figure 7e. However, as Figure 7f shows when combining MEGs 4 and 8 with OMME, and successively including higher MEGs, that artifact disappears. This is most likely to have happened since the dynamic range in the MEG 4 image is very close to the actual motion in that region, and hence wraps appear due to the noise.

The chessbox-like artifacts in the SWS map due to the directional filter in the preprocessing step are more noticeable in the volunteer data, see Figures 8a-8d, most likely due to the lower SNR compared to the phantom data. Stronger smoothing could remove the artifact but would also lead to further blurring of the images.

Finally, Figure 9 compares SWS maps reconstructed from wrap-free phase images of OMME using four MEGs, and Laplacian based unwrapping and Flynn unwrapping with the highest MEG. Additionally T2 weighted MRE magnitude images are shown for anatomical reference. Red arrows indicate areas where OMME based reconstruction clearly outperforms standard unwrapping procedures by fully recovering fluid/tissue boundaries between brain tissue and either ventricles or gyri.

4.3 Noise analysis

Figure 10 shows the results of the noise analysis for the phantom and in vivo data for the wrap-free wavefields recovered from Laplacian and Flynn phase unwrapping and OMME based unwrapping. Noise levels are decreasing with increasing MEG used as predicted by the theory. Noise levels for all three methods are similar. Interestingly the recovered signal power or displacement shows significant differences. For Laplacian and Flynn phase unwrapping the signal level is decreasing with increasing MEG strength and only shows a constant level for the OMME method. Since

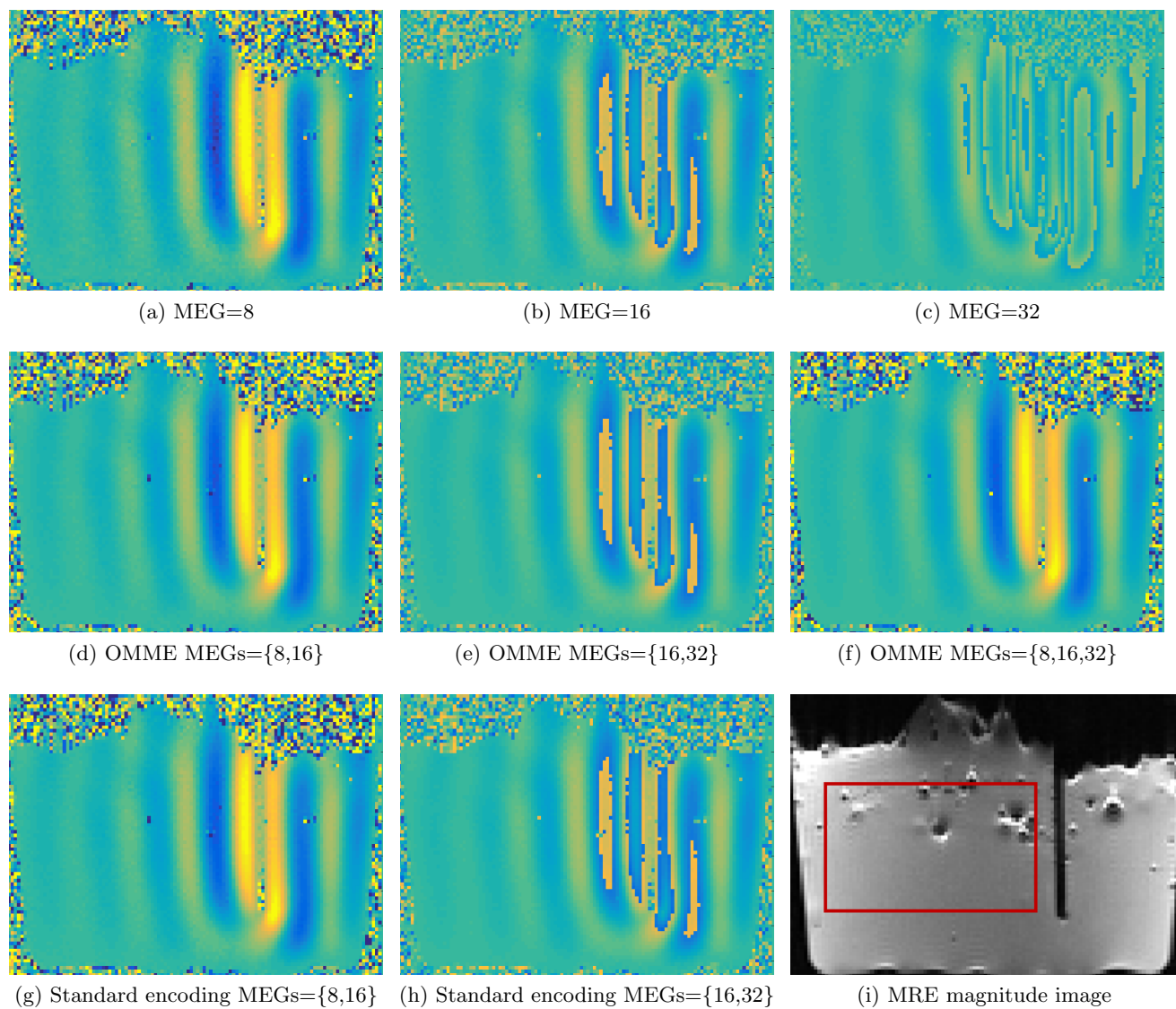


Figure 3: Multiple motion encoding reconstruction in the phantom. Color scale is set in the interval $\pm 80\%$ of the dynamic range of the MEG=8 image. Large positive values are coloured in yellow and negative values in blue, while green being zero. The last image shows the T2 weighted MRE magnitude as geometric reference.

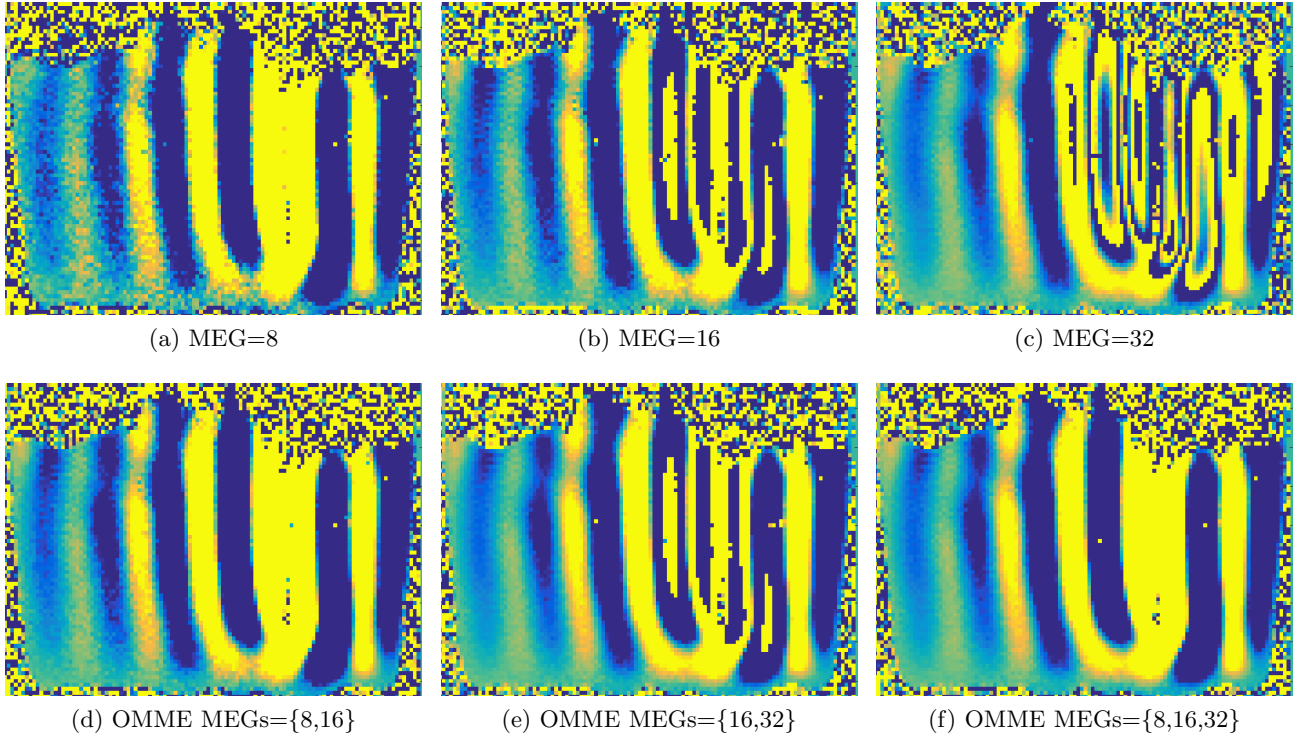


Figure 4: Multiple motion encoding reconstruction in the phantom. Colour scale is set in the interval $\pm 30\%$ the dynamic range of the MEG=32 image. Large positive values are colored in yellow and negative values in blue, while green being zero.

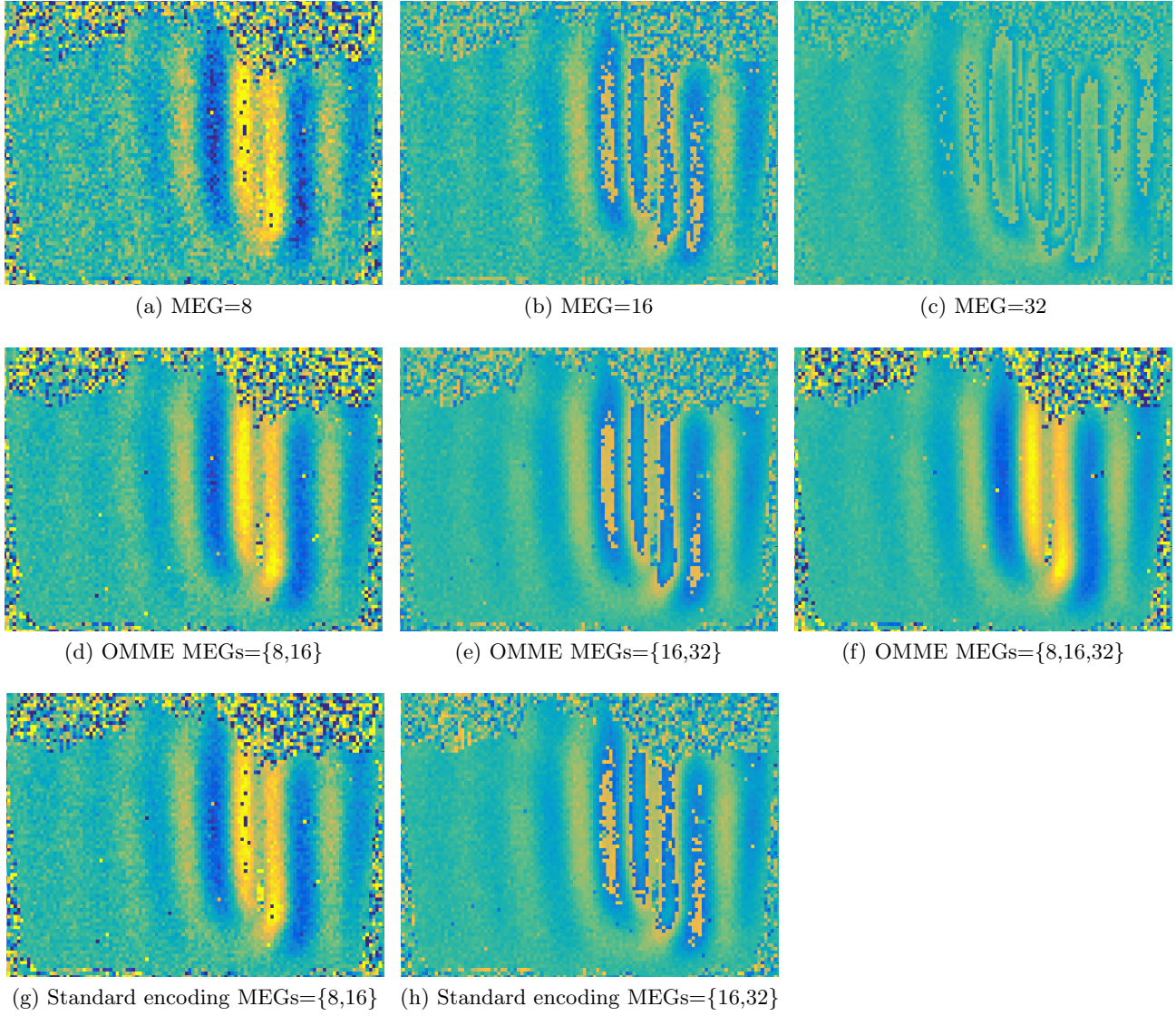


Figure 5: Multiple motion encoding reconstruction in the phantom with additional $\sigma_\varphi = 0.1$. Color scale is set in the interval $\pm 80\%$ of the dynamic range of the MEG=8 image. Large positive values are colored in yellow and negative values in blue, while green being zero.

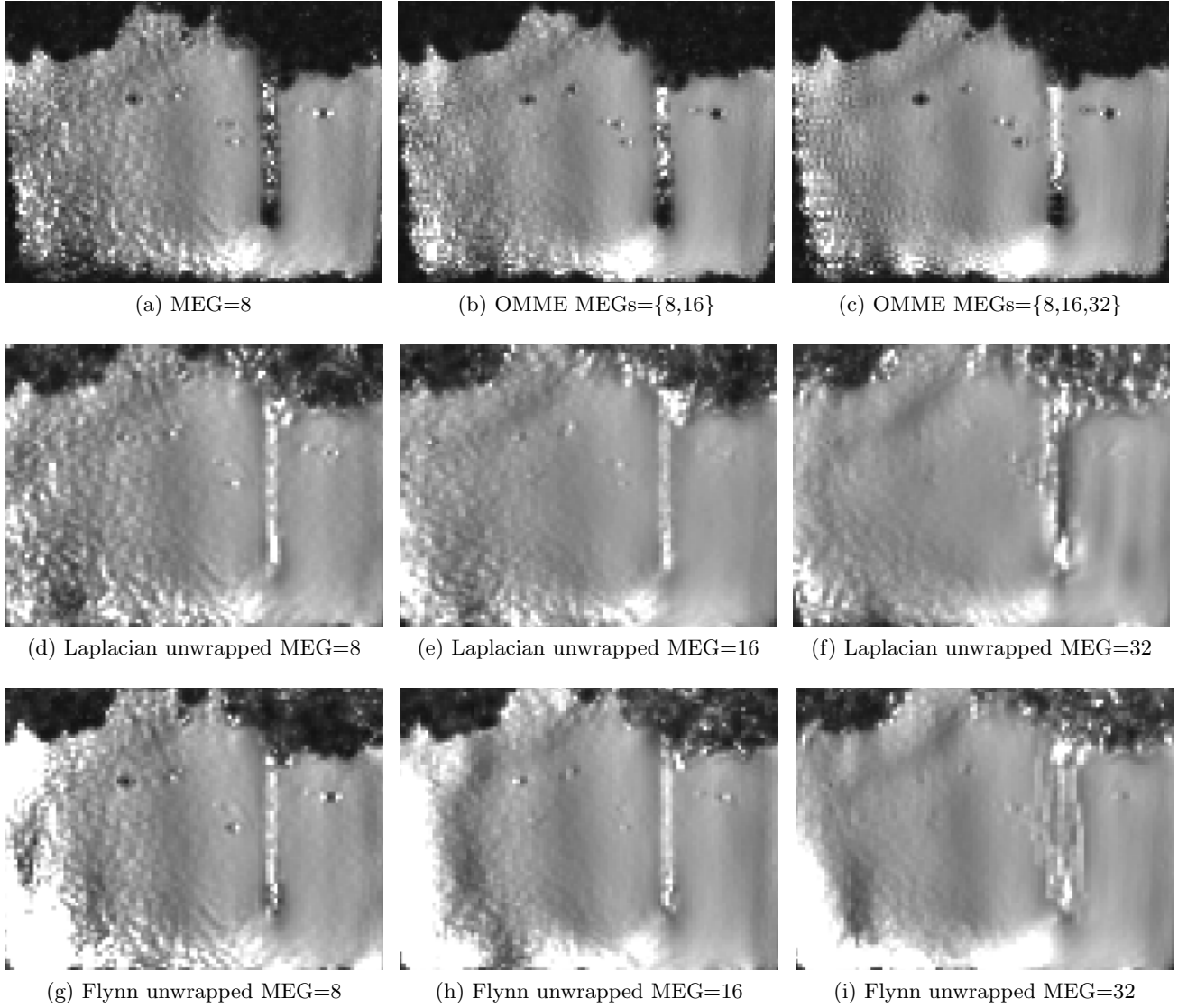


Figure 6: SWS maps reconstructed from k-MDEV at 30.03 Hz vibration frequency for a selected slice in the phantom. The excitation plate is visible on the right side. First row shows OMME results with one (a) to four (d) MEGs combined. The second row shows SWS recovered from Laplacian based unwrapped phase images with MEG of different strength. Last row shows SWS recovered from Flynn unwrapped phase images. Colorbar for SWS maps range from 0 to 1 m/s.

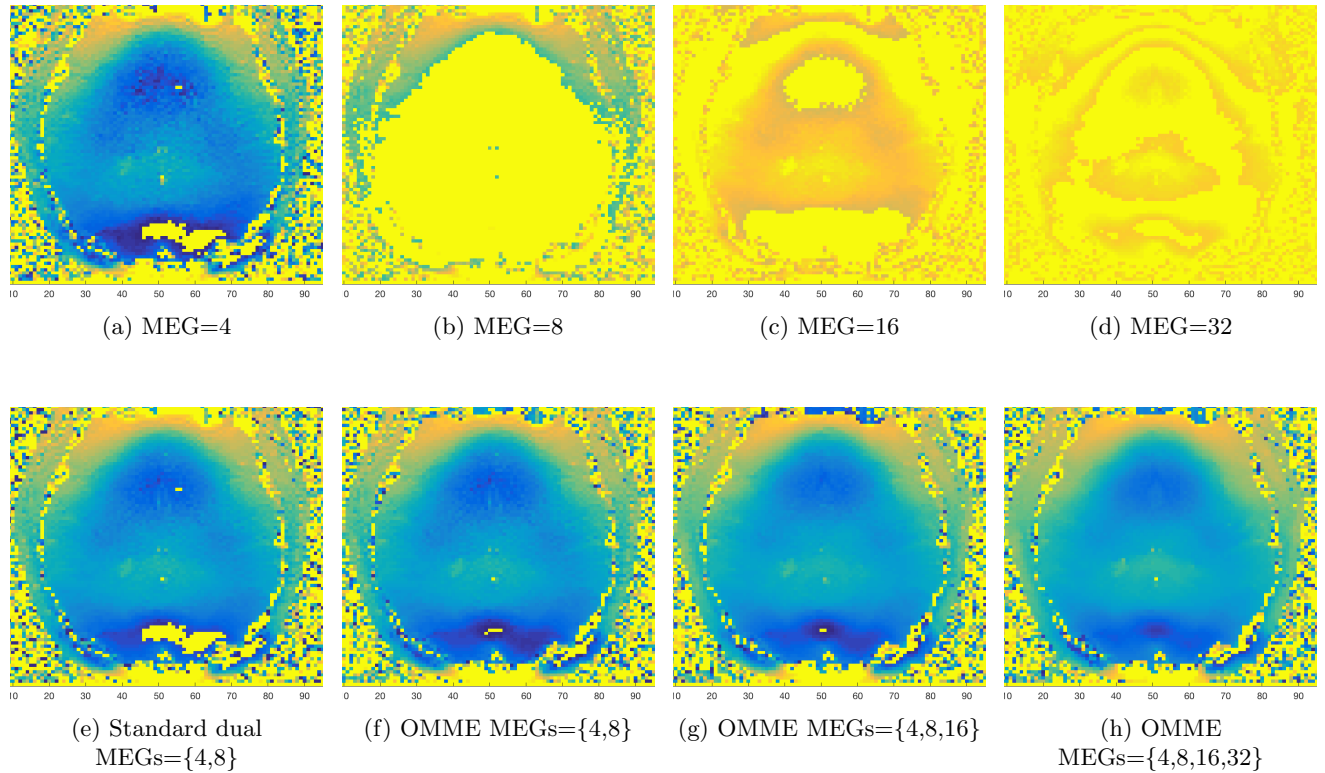


Figure 7: Multiple motion encoding reconstruction in the volunteer data. The first row shows phase images for a MEG acquisition with increasing MEG amplitude. The second row shows standard dual and OMME combined phase images with increasing amount of MEGs combined. Color scale is set in the interval between zero (bright yellow) and minus the dynamic range of the image with MEG=4 image (dark blue), hence the shift to yellow when wraps appear since the original image wave has mainly positive values.

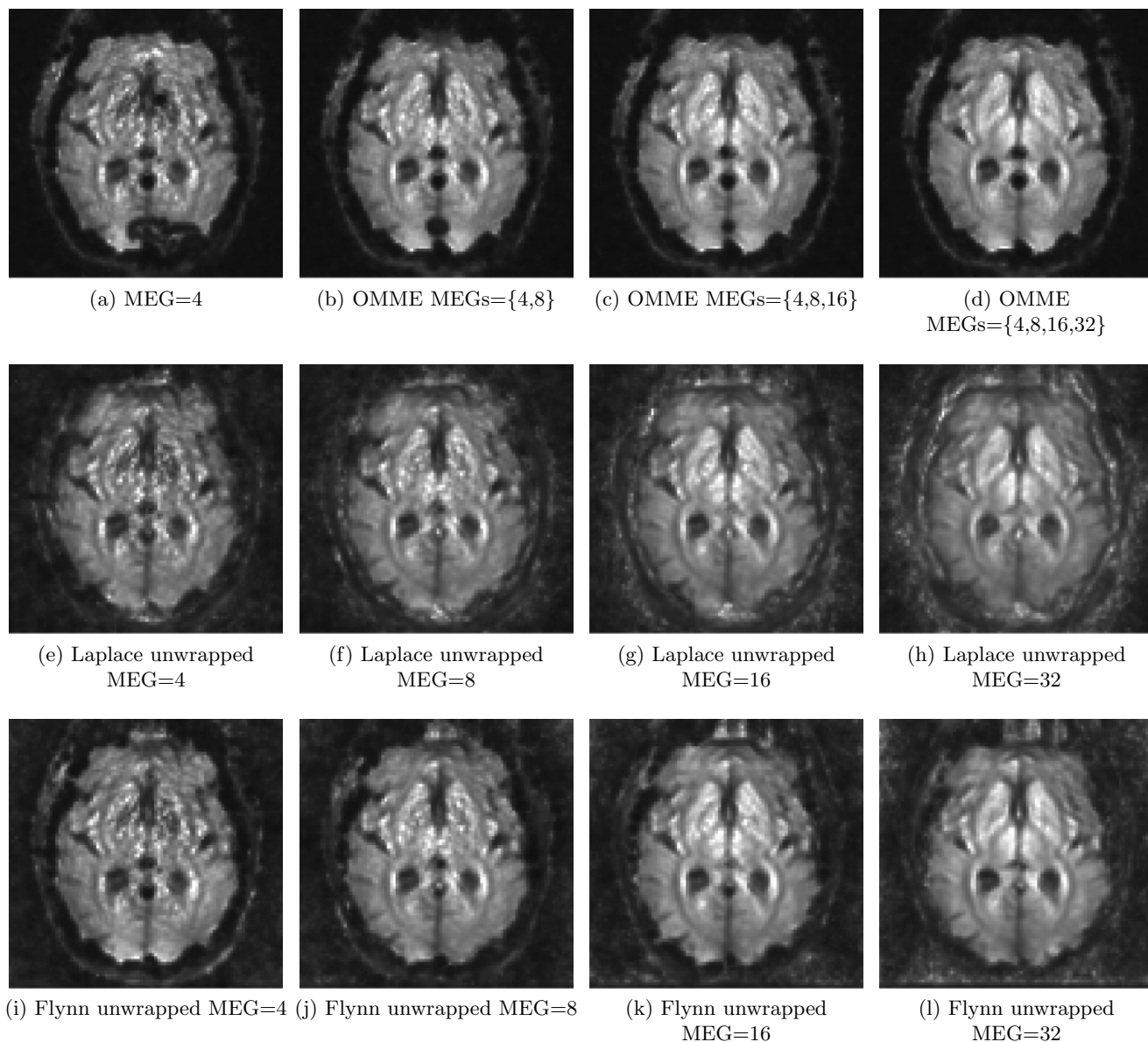


Figure 8: SWS maps for in vivo brain experiment at 25 Hz vibration frequency for a selected slice. First row shows OMME results with one (a) to four (d) MEGs combined. The second row shows SWS recovered from Laplacian based unwrapped phase images with MEG of different strength. Last row shows SWS recovered from Flynn unwrapped phase images. Colorbar for SWS maps range from 0 to 2 m/s.

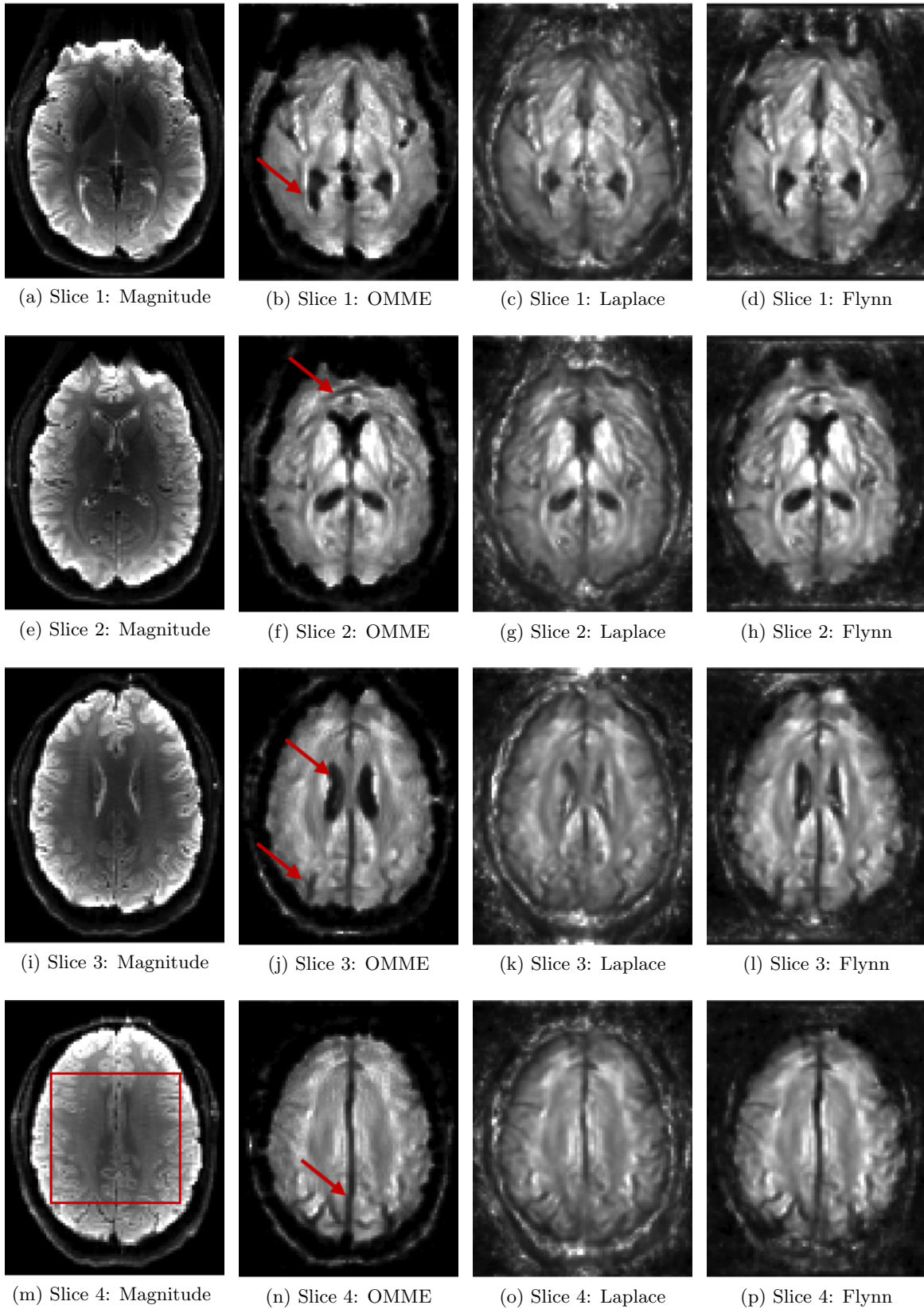


Figure 9: SWS maps for standard unwrapping (MEG=32) in comparison to OMME (MEGs={4,8,16,32}). Four selected slices show from left to right an anatomical reference image from T2 weighted MRE magnitude, SWS map based on wrap-free OMME phase, based on Laplacian unwrapped phase images and based on Flynn unwrapped phase images. Red arrows indicate areas where OMME outperforms the standard approaches. Colorbar for SWS maps range from 0.3 to 1.8 m/s.

the underlying displacement is the same for all MEG strengths, the signal power should also be constant. With similar noise but higher signal, OMME outperforms the other methods in terms of SNR.

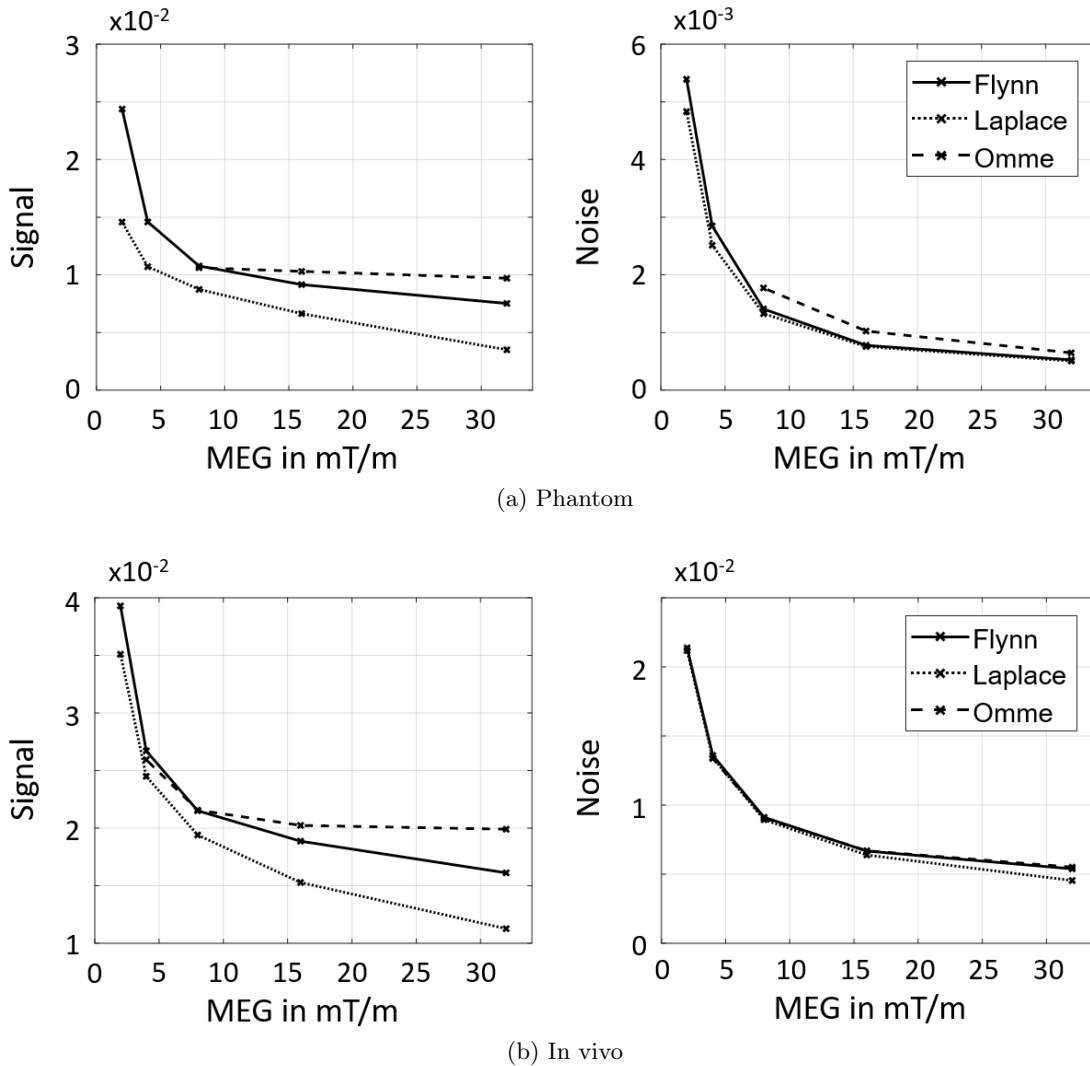


Figure 10: Signal (left) and noise (right) levels estimated from wavelet decomposition for all MEG strengths with Flynn and Laplacian unwrapping and OMME for (a) phantom data and (b) in vivo data. Signal and noise levels were averaged over all slices and components. For OMME, the data points indicate highest MEG used, i.e. at MEG 8, OMME used MEG 8 and 4; at MEG 16, OMME used MEG 16, 8 and 4; at MEG 32, OMME used MEG 32, 16, 8 and 4.

5 Discussion

We have developed, theoretically analyzed and assessed in numerical, phantom and volunteer data a new method for combining an arbitrary number of motion encoded PC images, the Optimal

Multiple Motion Encoding method (OMME). OMME was assessed using MRE measurements, but can be applied to other PC-MRI modalities as Flow MRI as it was done originally for the dual encoding case. To the best of the authors' knowledge, this is the first reported method to combine arbitrary number of motion encoded images with different MEGs.

For a fixed effective dynamic range of the imaged motion, OMME presents a superior performance with respect to noise compared to standard dual encoding unwrapping. This was assessed analytically and confirmed numerically in a "single voxel" experiment. The noise analysis for the experimental data confirm these findings.

It was concluded that the most robust strategy with respect to noise perturbations to combine N images was to measure dynamic ranges d_1, \dots, d_N such that $d_i = 2^{-i+1}d_1$. In practice, this combinations being fixed allows the scanner operator to easily select the largest dynamic range and number of measurements only, as it is usually done when selecting the signal averages, but now with a greater efficacy in MNR improvement with respect to the number of measurements.

The OMME was compared against standard unwrapping methods (Laplacian and Flynn). Remarkably, OMME allows to improve the SWS maps by reducing the noise in the wave images without spatial smoothing as Laplace unwrapping does and without unwrapping failure as it occurs with Flynn (predominantly at boundaries). This showed, in both phantom and volunteer data, to allow to capture details that either are considerably smoothed (out) by standard unwrapping methods. This can be extremely relevant for further pushing the ranges of higher resolution where MRE is applied to capture milder spatial variations of the tissue properties. It could be of potential value in future applications, for example to resolve small focal lesions as they occur in Multiple Sclerosis or to better resolve small stiffness contrasts in various applications. Moreover it is visible that standard unwrapping methods smear boundaries between fluid filled spaces and brain tissue. It not only effects the outer boundary of the brain but also transitions between tissue and fluid filled ventricles. If tissue mechanical properties are altered at those boundaries as it might be the case for Multiple Sclerosis OMME based wrap-free MRE phase images could have a great potential to be sensitive in those areas. At last, the increased dynamic range of OMME with good SNR properties could be utilized when high frequency vibrations induce heavy wraps near the source and get quickly damped with small deflection amplitudes inside the tissue under investigation. The potential OMME for high frequency brain MRE needs to be further investigated.

Concerning MRE, examination times are increased due to additional measurements necessary to acquire additional MEGs. Each additional MEG increases total scan time by the TA of one measurement. Moreover, the reference phase (i.e. MEGs on and vibration off) needs to be measured, which however is required at one time step only for all encoding directions, adding another $1/(\text{number of timesteps}) * \text{TA}$. But if phase wraps can be fully resolved, data impairment by unwrapping algorithms are avoided which can be critical for high resolution MRE. Even resolving wraps only partly prevents unwrapping algorithms from failure and allows high encoding efficiencies to capture damped waves without corrupting high amplitude regions.

Furthermore gains in MNR outperform regular averaging of multiple scans and possibly less data need to be acquired. In practical situations, scanner operators repeat scans if large wraps are seen by, e.g., reducing the vibration amplitude. OMME allows to keep the amplitude and continuously acquire (with different MEGs) and combine the images afterwards.

6 Conclusion

In this study, we proposed an optimal multiple motion encoding (OMME) method for any PC-MRI modality, including a detailed theoretical analysis. We applied this novel technique to MRE measurements and results are presented based on phantom and in vivo data. In MRE, OMME allows to recover better tissue details due to its increased MNR with a high dynamic range. This leads to SWS maps which preserve important details (e.g. discontinuities in the stiffness).

Especially for future applications of high resolution MRE when small features should be resolved, smoothing the wave image is undesired. For instance the mechanical characterization of focal demyelination of in vivo human brain tissue as it occurs in Multiple Sclerosis is not possible yet [27] and different attempts towards a finer resolution have already been investigated [8]. Application of OMME to other PC-MRI methods like e.g. Flow MRI might be investigated in future work.

conflict of interest

The authors declare no conflict of interest.

acknowledgments

H.H. and I.S. acknowledge the funding from the German Research Foundation (GRK 2260 BIOQIC, SFB1340 Matrix in Vision) and from the European Unions Horizon 2020 Program (ID 668039, EU FORCE Imaging the Force of Cancer). C.B. acknowledges the funding from the European Research Council (ERC) under the European Union’s Horizon 2020 research and innovation programme (grant agreement No 852544 - CardioZoom). A.O. acknowledge the funding of Conicyt Basal Program PFB-03, Fondecyt 1151512 and Fondap CR2-1511009. A.O and S.U. acknowledge funding from Millenium Science Initiative of the Ministry of Economy, Development and Tourism, grant Nucleus for Cardiovascular Magnetic Resonance. S.U. also thanks to Fondecyt 1181057.

References

- [1] Eric Barnhill, Lyam Hollis, Ingolf Sack, Jürgen Braun, Peter R Hoskins, Pankaj Pankaj, Colin Brown, Edwin JR van Beek, and Neil Roberts. Nonlinear multiscale regularisation in mr elastography: Towards fine feature mapping. *Medical image analysis*, 35:133–145, 2017.
- [2] Eric Barnhill, Paul Kennedy, Curtis L Johnson, Marius Mada, and Neil Roberts. Real-time 4d phase unwrapping applied to magnetic resonance elastography. *Magnetic resonance in medicine*, 73(6):2321–2331, 2015.
- [3] Gergely Bertalan, Jing Guo, Heiko Tzschätzsch, Charlotte Klein, Eric Barnhill, Ingolf Sack, and Jürgen Braun. Fast tomoelastography of the mouse brain by multifrequency single-shot mr elastography. *Magnetic resonance in medicine*, 81(4):2676–2687, 2019.
- [4] Fraser Callaghan, Rebecca Kozor, Andrew Sherrah, Michael Vallely, David Celermajer, Gemma Figtree, and Stuart Grieve. Use of multi-velocity encoding 4d flow mri to improve quantification of flow patterns in the aorta. *Journal of Magnetic Resonance Imaging*, 43(2):352–363, 2016.

- [5] H. Carrillo, A. Osses, S. Uribe, and C. Bertoglio. Optimal dual-vent (odv) unwrapping in phase-contrast mri. IEEE Transactions on Medical Imaging, 38:1263–1270, 2019.
- [6] Florian Dittmann, Rolf Reiter, Jing Guo, Matthias Haas, Patrick Asbach, Thomas Fischer, Jürgen Braun, and Ingolf Sack. Tomoelastography of the prostate using multifrequency mr elastography and externally placed pressurized-air drivers. Magnetic resonance in medicine, 79(3):1325–1333, 2018.
- [7] David L Donoho, Iain M Johnstone, Gérard Kerkyacharian, and Dominique Picard. Wavelet shrinkage: asymptopia? Journal of the Royal Statistical Society: Series B (Methodological), 57(2):301–337, 1995.
- [8] Andreas Fehlner, Janina Ruth Behrens, Kaspar-Josche Streitberger, Sebastian Papazoglou, Jürgen Braun, Judith Bellmann-Strobl, Klemens Ruprecht, Friedemann Paul, Jens Würfel, and Ingolf Sack. Higher-resolution mr elastography reveals early mechanical signatures of neuroinflammation in patients with clinically isolated syndrome. Journal of Magnetic Resonance Imaging, 44(1):51–58, 2016.
- [9] Thomas J Flynn. Two-dimensional phase unwrapping with minimum weighted discontinuity. JOSA A, 14(10):2692–2701, 1997.
- [10] Sebastian Hirsch, Ingolf Sack, and Jürgen Braun. Magnetic resonance elastography: physical background and medical applications. John Wiley & Sons, 2017.
- [11] Dieter Klatt, Uwe Hamhaber, Patrick Asbach, Jürgen Braun, and Ingolf Sack. Noninvasive assessment of the rheological behavior of human organs using multifrequency mr elastography: a study of brain and liver viscoelasticity. Physics in Medicine & Biology, 52(24):7281, 2007.
- [12] Adrian Lee, Bruce Pike, and Norbert Pelc. Three-point phase-contrast velocity measurements with increased velocity-to-noise ratio. Magnetic Resonance in Medicine, 33:122–128, 1995.
- [13] Michael Loecher, Eric Schrauben, Kevin Johnson, and Oliver Wieben. Phase unwrapping in 4d mr flow with a 4d single-step laplacian algorithm. Journal of Magnetic Resonance Imaging, 43(4):833–842, 2016.
- [14] Gavin Low, Scott A Kruse, and David J Lomas. General review of magnetic resonance elastography. World journal of radiology, 8(1):59, 2016.
- [15] A Manduca, DS Lake, KT Huynh, RS Eon, EM Annoni, and RL Ehman. Consistent snr measures for magnetic resonance elastography. In Proceedings of the 23rd Annual Meeting of ISMRM, Toronto, Canada, volume 2519, 2015.
- [16] Yogesh K Mariappan, Kevin J Glaser, and Richard L Ehman. Magnetic resonance elastography: a review. Clinical anatomy, 23(5):497–511, 2010.
- [17] MDJ McGarry, EEW Van Houten, PR Perrinez, AJ Pattison, JB Weaver, and KD Paulsen. An octahedral shear strain-based measure of snr for 3d mr elastography. Physics in Medicine & Biology, 56(13):N153, 2011.

- [18] Joaquin Mura, Felix Schrank, and Ingolf Sack. An analytical solution to the dispersion-by-inversion problem in magnetic resonance elastography. Magnetic Resonance in Medicine, 84(1):61–71, 2020.
- [19] Kay M Pepin, Richard L Ehman, and Kieran P McGee. Magnetic resonance elastography (mre) in cancer: technique, analysis, and applications. Progress in nuclear magnetic resonance spectroscopy, 90:32–48, 2015.
- [20] Ingolf Sack, Jens Rump, Thomas Elgeti, Abbas Samani, and Jurgen Braun. Mr elastography of the human heart: Noninvasive assessment of myocardial elasticity changes by shear wave amplitude variations. Magnetic Resonance in Medicine, 61(3):668–677, 2008.
- [21] Susanne Schnell, Sameer Ansari, Can Wu, Julio Garcia, Ian Murphy, Ozair Rahman, Amir Rahsepar, Maria Aristova, Jeremy Collins, James Carr, and Michael Markl. Accelerated dual-ventricle 4d flow mri for neurovascular applications. Journal of Magnetic Resonance Imaging, 46:102–114, 2017.
- [22] Marvin A Schofield and Yimei Zhu. Fast phase unwrapping algorithm for interferometric applications. Optics letters, 28(14):1194–1196, 2003.
- [23] Felix Schrank, Carsten Warmuth, Heiko Tzschätzsch, Bernhard Kreft, Sebastian Hirsch, Jürgen Braun, Thomas Elgeti, and Ingolf Sack. Cardiac-gated steady-state multifrequency magnetic resonance elastography of the brain: Effect of cerebral arterial pulsation on brain viscoelasticity. Journal of Cerebral Blood Flow & Metabolism, 40(5):991–1001, 2020.
- [24] Ivan W Selesnick, Richard G Baraniuk, and Nick C Kingsbury. The dual-tree complex wavelet transform. IEEE signal processing magazine, 22(6):123–151, 2005.
- [25] Siddharth Singh, Sudhakar K Venkatesh, Zhen Wang, Frank H Miller, Utaroh Motosugi, Russell N Low, Tarek Hassanein, Patrick Asbach, Edmund M Godfrey, Meng Yin, et al. Diagnostic performance of magnetic resonance elastography in staging liver fibrosis: a systematic review and meta-analysis of individual participant data. Clinical Gastroenterology and Hepatology, 13(3):440–451, 2015.
- [26] Monvadi Srichai, Ruth Lim, Samson Wong, and Vivian Lee. Cardiovascular applications of phase-contrast mri. American Journal of Roentgenology, 192(3):662–675, 2009.
- [27] Kaspar-Josche Streitberger, Ingolf Sack, Dagmar Krefting, Caspar Pfüller, Jürgen Braun, Friedemann Paul, and Jens Wuerfel. Brain viscoelasticity alteration in chronic-progressive multiple sclerosis. PloS one, 7(1):e29888, 2012.
- [28] Heiko Tzschätzsch, Jing Guo, Florian Dittmann, Sebastian Hirsch, Eric Barnhill, Korinna Jöhrens, Jürgen Braun, and Ingolf Sack. Tomoelastography by multifrequency wave number recovery from time-harmonic propagating shear waves. Medical image analysis, 30:1–10, 2016.
- [29] John B Weaver, Elijah EW Van Houten, Michael I Miga, Francis E Kennedy, and Keith D Paulsen. Magnetic resonance elastography using 3d gradient echo measurements of steady-state motion. Medical physics, 28(8):1620–1628, 2001.

- [30] Ziyang Yin, Yi Sui, Joshua D Trzasko, Phillip J Rossman, Armando Manduca, Richard L Ehman, and John Huston III. In vivo characterization of 3d skull and brain motion during dynamic head vibration using magnetic resonance elastography. Magnetic resonance in medicine, 80(6):2573–2585, 2018.